Journal of Power Sources 531 (2022) 231327

Contents lists available at ScienceDirect

Journal of Power Sources

journal homepage: www.elsevier.com/locate/jpowsour

Quantification of lithium inventory loss in micro silicon anode via titration-gas chromatography

Bhagath Sreenarayanan [a], Darren H.S. Tan [a], Shuang Bai [b], Weikang Li [a], Wurigumula Bao [a,**], Ying Shirley Meng [a,b,c,*]

[a] Department of NanoEngineering, University of California San Diego, La Jolla, CA, 92093, USA
[b] Materials Science and Engineering, University of California San Diego, La Jolla, CA, 92093, USA
[c] Pritzker School of Molecular Engineering, University of Chicago, Chicago, IL, 60637, USA

HIGHLIGHTS

- Titration gas chromatography can quantify the Li inventory loss in silicon anode.
- The formation of Li–Si alloy upon lithiation leads to a non-linear volume expansion.
- Robust binder and state of charge control can reduce trapped Li–Si amount.

GRAPHICAL ABSTRACT

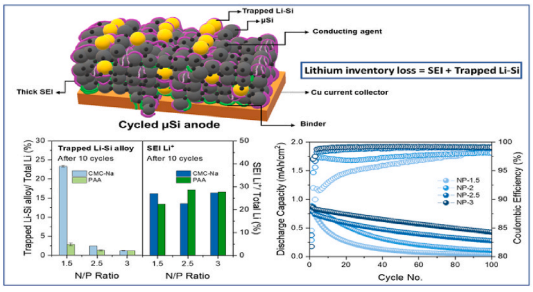

ARTICLE INFO

Keywords:
Lithium-ion battery
Silicon anode
Titration gas chromatography
Solid electrolyte interphase
Trapped Li–Si Alloy

ABSTRACT

The commercialization of silicon as an anode material for lithium-ion batteries has been largely impeded by its severe volume changes during cell operation, causing continuous loss of Li inventory. As such, it is vital to understand and quantify the sources of capacity fade in order to design effective mitigation strategies. Herein, we design a method based on Titration Gas Chromatography (TGC) to reveal a non-linear volume expansion in μSi anode during the lithiation process. The severe volume expansion towards the end of lithiation leads to accelerated SEI formation and conductive pathway loss, resulting in a large amount of trapped Li–Si alloy accumulation. The TGC method is also applied to investigate μSi anodes with two different binders: Sodium Carboxymethyl Cellulose (CMC-Na) and Polyacrylic Acid (PAA). The primary reason for capacity loss for anode with CMC-Na binder is trapped Li–Si alloy, which can be mitigated by using more robust PAA binder. The Sate of Charge (SoC) control principle is also investigated in μSi-LFP full cells with both binders by tuning the N/P ratios (1.5–3). The results indicate binder robustness is crucial for mitigating the trapped Li–Si alloy accumulation in μSi anode.

** Corresponding author.
* Corresponding author. Department of NanoEngineering, University of California San Diego, La Jolla, CA, 92093, USA
E-mail addresses: wubao@eng.ucsd.edu (W. Bao), shmeng@ucsd.edu (Y.S. Meng).

https://doi.org/10.1016/j.jpowsour.2022.231327
Received 14 January 2022; Received in revised form 4 March 2022; Accepted 15 March 2022
Available online 22 March 2022

1. Introduction

Alloy-based materials are increasingly used as anode candidates due to its potential to increase energy densities of LIBs. Among them, silicon stands out as a material because of its low cost and relative abundance within the earth's crust (second most abundant element by volume of earth's crust) [1] [–] [3]. In addition, silicon also possesses high theoretical specific capacity (3579 mAh/g) and low working potential (0.4 V vs. Li/Li^+), which are key features to enable high energy-density LIBs [2]. However, major roadblocks toward commercialization of silicon-based anodes include its severe volume expansion during electrochemical cycling, which leads to continuous SEI formation and Li inventory losses [4]. At the particle level, the stress-strain effects caused by the severe volume expansion induces cracks within larger particles, exposing new surfaces to the electrolyte, resulting in decomposition to form additional SEI [4]. Previous studies have shown a strong dependence on particle size in the propagation of cracks, where a small critical diameter (D_c ~150 nm) was found to be essential in mitigating crack propagation [5–7]. On the electrode scale, severe volume expansion leads to the loss of electrical contact between the active material and conductive network, resulting in an accumulation of trapped Li–Si alloy within the electrode matrix [4,8,9]. Fig. 1 summarizes the major challenges of μSi anode for LIBs.

In the past, several groups have employed various characterization tools to study the failure mechanisms in silicon anodes. Oumellal et al. [10] used ex-situ ^{7}Li MAS NMR to show that most Li losses are found on the surface of the nano silicon particle in the form of SEI products. Rhodes et al. [11] employed a semi-quantitative Acoustic Emission technique (AE) to understand the nature of crack formation and also the time of occurrence of crack formation and propagation during the lithiation and de-lithiation processes in μSi anode. Most emission signals were detected in the first lithiation cycle, corresponding to new surface cracking in the initial lithiation process. Gonzalez et al. [12] used X-Ray micro-computed tomography (X-Ray micro-CT) to visualize the μSi particle expansion, crack propagation, and pore formation due to gas production from side reactions caused by the electrolyte decomposition. Most of these studies have focused on the qualitative or semi-quantitative description of SEI and its properties. Little attention was given to the Li inventory loss quantification at the μSi anode, especially in the context of a full cell with limited Li source. Most reported literature conducted studies on half-cells using an infinite Li source, making quantification of Li losses challenging. Moreover, most advanced characterization tools are limited to pure silicon systems such as silicon thin films, silicon nanowires/nanorods, etc. [13–16]. It is vital to develop quantification tools to analyze practical electrode systems where inactive components such as binders and conductive agents present can affect Li inventory losses.

To reduce the Li inventory loss in silicon anodes, several mitigation strategies have been previously proposed. These methods can be mainly classified into three broad categories: morphological designs, electrolyte additives, and novel binders. Different silicon morphologies such as nano-wires [17], nano-layers [18], core-shell model [19], and yolk-shell model [20] have been utilized to reduce the net volume expansion-contraction stress induced by distributing it throughout the structure. As for electrolyte additives, fluoroethylene carbonate (FEC [21,22]) and vinylene carbonate (VC [23]) have been reported to form a robust passivating SEI layer consisting of LiF, Li_2O, Li_2CO_3, which improved the cycle stability of silicon anode. Apart from carbonate ester solvents, additives such as succinic anhydride (SA [24]), tetraethoxysilane, and (2-cyanoethyl)-triethoxysilane (TEOS and TEOSCN [25]) have also been reported. In exploring novel binders, co-polymer binders like alginate binder [26], cross-linking type such as polyacrylic acid-carboxymethyl cellulose (PAA-CMC [27]), self-healing polymeric binders such as Meldrum's acid-based functional binder [28], conducting polymeric binders such as PEFM functional binder [29] have been reported. These novel binders have been shown to reduce the capacity fade upon cycling by maintaining sufficient conductive network within the entire electrode. While different characterization techniques have been performed in these reports, they still largely focused on the qualitative aspects of interfacial and mechanical stability. However, quantitative results to determine how these proposed strategies can influence the Li inventory losses have yet to be revealed.

Our earlier work on silicon thin film anodes using Titration Gas Chromatography (TGC) method quantitatively confirmed the trapped

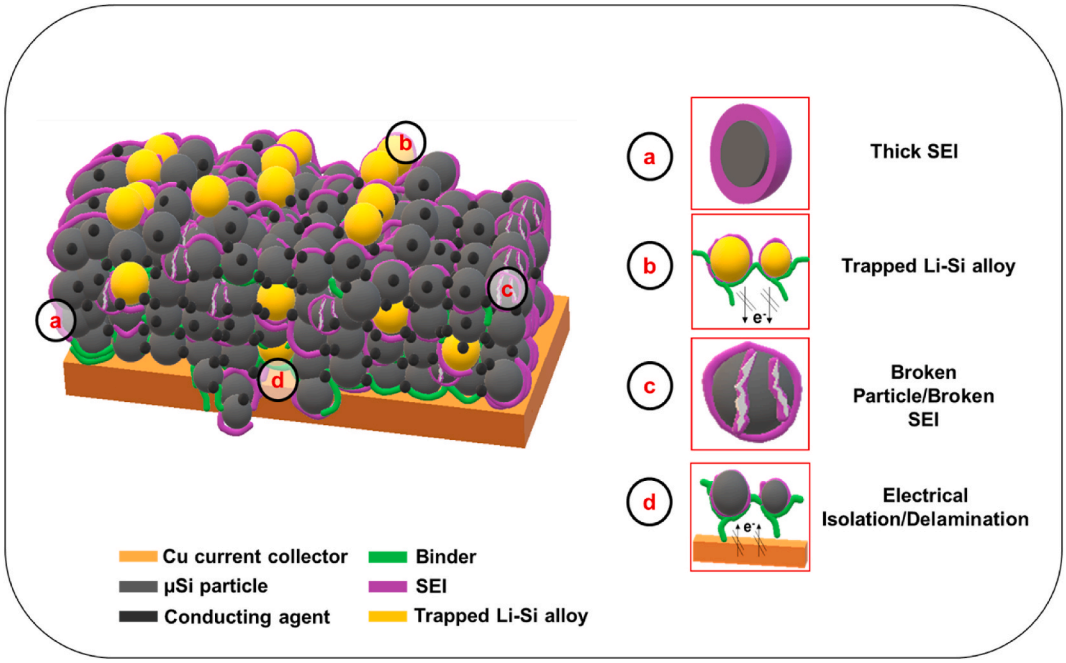

Fig. 1. Challenges of μSi anode for LIBs: (a) **Thick SEI**: continuous exposure of new surface to the electrolyte results in dynamic SEI (b) **Trapped Li–Si alloy**: thick SEI isolates the electronic pathway for the de-alloying process (c) **Broken SEI/Broken Particle**: continuous volume expansion-contraction results in pulverization of particles and broken SEI (d) **Electrical Isolation/Delamination**: continuous volume expansion-contraction cycles lead to electrical isolation of active material.

Li–Si alloy formation due to high volume expansion-contraction cycles [30]. In this work, Titration Gas Chromatography (TGC) method has been successfully implemented to μSi electrode, which contained both binder and carbon conductive agent. The SEI formation process at the first cycle was quantitatively studied with the evolution of SEI and trapped Li–Si amount upon cycling in half cells and full cells when using different binders. It was also identified that employing the state of charge control (SoC) by increasing the N/P ratio in the full cell can reduce the trapped Li–Si when using CMC-Na as the binder. Also, the trapped Li–Si amount was drastically reduced when PAA was used as the anode binder. The TGC method allows us to quantitatively distinguish the loss of active lithium consumed by SEI formation and the trapped Li–Si alloy caused by the kinetic limitations and contact losses.

2. Experimental methods

2.1. Sample preparation

The anodes consisted of commercial μSi (1–5 μm, Alfa Aesar) or Nano Si (<50 nm, Alfa Aesar) as the active material (70% by weight), Acetylene carbon black (AB, Strem Chemicals) as a conductive additive (20% by weight), and CMC-Na (Mw 250,000, Sigma Aldrich) or PAA (Mv 450,000, Sigma Aldrich) as binders (10% by weight). The electrode cast mixture was dispersed in water and then mixed using a Thinky Mixer at 2000 rpm for 40 min. The obtained slurry was cast onto a copper foil using Doctor blade and was dried for 12 h at 80 °C under vacuum to remove the water. After the cast was dried, electrodes with varying diameters, 3/8 inch for half-cell and 13 mm for the full cell, were punched from the casts. The $LiFePO_4$ (LFP) cathode for the full cell was purchased from NEI (Areal capacity ~ 1.25 mAh/cm^2, diameter 1/2 inch). For the N/P ratio control study, μSi anode cast with different areal loading: 1.9 mAh/cm^2, 2.5 mAh/cm^2, 3.1 mAh/cm^2, 3.8 mAh/cm^2 were cast onto the copper foil.

2.2. Electrochemical test

For the half-cell testing, the μSi electrode or Nano Si electrode was assembled into a 2032 type coin cell. Li metal (1 mm thick) was employed as the counter electrode. The electrolyte was 1 mol/L $LiPF_6$ dissolved in ethylene carbonate (EC): diethyl carbonate (DEC) (1:1 by weight) with 10% fluoroethylene carbonate (FEC) (Gotion). The half-cell was cycled between 50 mV and 1.5 V at room temperature at a current density (1C = 3500 mA/g) of C/20 during the first cycle and C/10 for subsequent cycles. For the full cell testing, the μSi electrode was paired with an LFP cathode and assembled in a 2032 type coin cell. The full cell was cycled between 2 V and 3.6 V at room temperature at a current density (1C = 170 mAh/g, based on LFP) of C/10 for the first two cycles and C/3 for the subsequent cycles. All the coin cells were assembled in the Ar-filled glovebox and tested on the NeWare battery cycler.

2.3. Characterizations

Titration Gas Chromatography (TGC): The TGC experiments were performed using a Shimadzu GC-2010 Plus Tracera equipped with a barrier ionization discharge (BID) detector. The Split temperature was kept at 200 °C with a split ratio of 2.5 (split vent flow: 20.58 ml/min, column gas flow: 8.22 ml/min, purge flow: 0.5 ml/min). Column temperature (RT-Msieve 5A, 0.53 mm) was kept at 40 °C, and the BID detector was held at 235 °C. Helium (99.9999%) was used as the carrier gas, and the BID detector gas flow rate was 50 ml/min. The electrode sample was put in a septum sealed glass vial. After injecting the 0.5 mL ethanol (200 proof anhydrous), the sample gases (30 μL) were injected into the machine via a 50 μL Gastight Hamilton syringe.

Scanning Electron Microscopy (SEM): The SEM was conducted on the FEI Apreo SEM; the coin cells were disassembled in the Ar-filled glovebox after cycling. The samples were transferred to the SEM chamber for cross-section analysis with minimal exposure to air. The electron beam operating voltage was 5 kV, and the operating current was 0.1 nA.

180° Peel-off Test: 180° Peel-off Test was performed using Instron Load Frame B. The two binder casts—PAA and CMC-Na were prepared at high mass loading (5.5 mAh/cm^2) with the same weight percentage of active material, conducting agent, and binder (70:20:10) used for the electrochemical tests. Before the test, the two casts were cut into 30 mm wide, 70 mm long specimens. The thickness of the specimen was 55 μm. The Kapton® tape was then attached to the specimen. This tape was peeled off using the Instron Load Frame B mechanical testing machine. The cross-head speed used for the test was 200 mm/min. During the peel-off process, a load v/s displacement plot was recorded to determine the adhesion strength of the binder to the copper current collector.

X-Ray Photoelectron Spectroscopy (XPS): X-ray photoelectron spectroscopy (XPS) was performed using a Kratos AXIS Supra. All samples were prepared without washing while transferred without air exposure. An Al anode source at 15 kV with a 10-8 Torr vacuum level was applied for measurement. The step size for Survey scans was 1.0 eV, followed by high-resolution scans with a step size of 0.1 eV. C 1s peak at 284.6 eV was used for calibration. The etching condition used was Ar + mono mode, 5 keV voltage.

3. Results and discussion

3.1. Establishing TGC method for μSi electrodes

To ensure that results generated from the quantification study are valid, several control experiments were performed to verify ethanol as a suitable solvent for the TGC study. Our previous work demonstrated that ethanol could be used as the titrant for the silicon thin film in the TGC study [30]. However, the reactivity of conducting agent and binder with ethanol has yet to be verified. Half cells were first assembled using electrodes with CMC-Na binder and CMC-Na with AB. The μSi electrode was also tested as the reference here. The half cells were discharged to 0.01 V with a current density of 0.1 mA/cm^2 (Fig. S1 (a)) and then disassembled to perform the TGC test. From the TGC data, H_2 gas was not detected from the binder-only electrode (Fig. S1 (c)), indicating that CMC-Na would not produce any H_2 gas with ethanol. While some H_2 gas was detected from the CMC-Na + AB electrode, this was 2 orders of magnitude lower than the expected amount from the μSi electrode. Furthermore, CMC-Na + AB after 1 cycle was verified with the TGC titrant, and the results are presented in Fig. S1 (b). In the case of μSi electrode, a large amount of H_2 gas was detected due to the presence of the Li–Si alloy formed during lithiation of μSi. Thus, it can be concluded that most H_2 gas detected in the μSi electrode should come from the Li–Si alloy, according to equation (1) below. The H_2 amount can be quantified by the GC machine based on the calibration curve we built in our previous work [30]. Therefore, the SEI amount can be obtained based on equation (2).

$$2\,Li_xSi\,(s) + 2x\,H^+\,(aq.) = 2x\,Li^+\,(aq.) + 2\,Si\,(s) + x\,H_2\,(g) \quad (1)$$

$$\text{Li loss (from cycler)} = \text{Trapped Li–Si alloy (from GC)} + \text{SEI Li}^+ \quad (2)$$

4. Quantifying Li–Si alloy & SEI growth

To study the evolution of Li–Si alloy and SEI formation, TGC was performed at different lithiation states (PLX, where X = 1,2, 3 …) by controlling the cut-off capacity for the μSi electrode, and the results are shown in Fig. 2 (b). It is worth noting that no H_2 gas could be detected until 0.15 V (corresponds to PL4), indicating that the initial capacity fully corresponds to only SEI formation. This result also indicates that

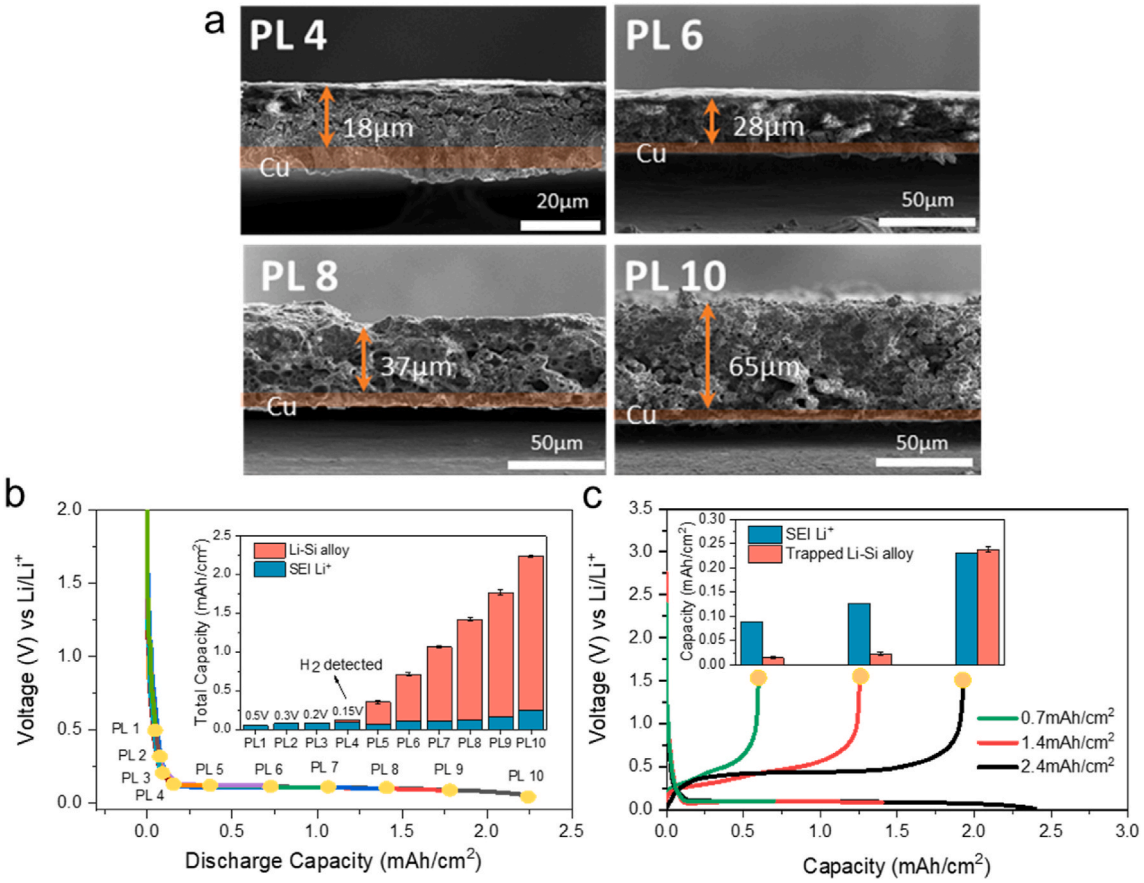

Fig. 2. (a) SEM cross-section images of points of lithiation: PL4, PL6, PL8, PL10 (b) First lithiation process in µSi electrode from half-cell; **inset:** related TGC Data (c) First cycle voltage profile of µSi electrode with different lithiation capacities; **inset:** related TGC result after de-lithiation.

the alloying reaction commenced when the voltage (vs. Li/Li^+) reached between 0.2 V and 0.15 V (corresponds to PL4 and PL3, respectively). Upon analyzing the SEM images of the cross-section (Fig. 2 (a) and Fig. S2), it can be seen that the electrode is expanding non-linearly with respect to lithiation capacity from PL4 till the end of lithiation at PL10. Additionally, TGC results from PL4 to PL10 (Fig. 2 (b)-inset) show that SEI is increasing with further lithiation, with the largest increase at PL9 & 10. As the rate of SEI formation is correlated with any new surfaces being formed, this indicates a non-linear volume expansion of the electrode during lithiation. As the largest degree of volume change occurs toward the end of lithiation (PL9 & 10), it can be inferred that most capacity losses would occur within these regions. To verify this, a control experiment was set up to understand the impact of non-linear volume change on irreversible capacity loss. The half cells were cycled for one cycle with 3 different lithiation capacities: 0.7 mAh/cm^2, 1.4 mAh/cm^2 and 2.4 mAh/cm^2. From the electrochemical data as shown in Fig. 2 (c), it can be seen that the initial coulombic efficiency (ICE) was lowest for the cell with a lithiation capacity of 2.4 mAh/cm^2, which was 80.42%, and highest for the cell with lithiation capacity of 0.7 mAh/cm^2 which was 85.16%. Moreover, from Fig. 2 (c)-inset, the trapped Li–Si, and SEI were lowest for the cell with a lithiation capacity of 0.7 mAh/cm^2 and highest for the cell with a lithiation capacity of 2.4 mAh/cm^2. Therefore, this result shows that the irreversible Li inventory loss can be reduced if the regions of largest volume expansion in µSi electrodes can be avoided.

4.1. Binder and active material particle size effects on Li inventory losses

As robust binders are commonly proposed as a solution to mitigate capacity losses, the TGC tool was also applied to analyze the effects of two commonly used binders in µSi electrodes: PAA and CMC-Na. From the cycle performance of CMC-Na half cell and PAA half cell in Fig. 3 (a), it can be seen that the capacity retention was only 4.5% for CMC-Na half cell after 50 cycles. In contrast, in the case of PAA half cell, the capacity retention was 76.6% after 50 cycles. Also, the average CE over 50 cycles for CMC-Na half cell and PAA half cell were 97.2% and 98.8% respectively. From the TGC data in Fig. 3 (b,c), it is seen that both cells exhibited a similar degree of SEI formation. However, the total capacity loss of CMC-Na half cell is higher than that of PAA half cell at every cycle, mainly attributed to accumulation of trapped Li–Si alloy. The binder effect on SEI was further studied using XPS depth profiling (Figs. S4 and S5). From the XPS depth profiling data, it can be observed that LiF in the F 1s spectrum was seen at the surface (0 min) and also after 2 min of etching for PAA and CMC-Na binders. Also, the other inorganic species: Li_2O was seen on the surface and also after 2 min of etching which was confirmed from O 1s spectra and Li 1s spectra. Similar observations can be seen for O 1s spectra, Li 1s spectra and C 1s spectra regarding the carbonaceous species such as ROLi (corresponding to 531 eV in O 1s and 55 eV in Li 1s), C═O (corresponding to 530 eV in O 1s and 287 eV in C 1s), C–O (corresponding to 286 eV in C 1s and 532 eV in O 1s), C–C (corresponding to 285 eV in C 1s), consistent with earlier study of SEI components on Nano Si anode by Radvanyi et al. [31], suggesting a mixed organic and inorganic SEI of similar compositions in PAA and CMC-Na binders. Thus, it can be inferred that the capacity losses due to SEI is not affected by the type of binder used. Conversely, the degree of trapped Li–Si alloy in the half cells for the extended cycles is highly influenced by the type of binder used. Particle size reduction is a commonly proposed strategy to mitigate capacity losses. To test the impact of active material particle size on Lithium inventory losses, the TGC tool was used in Nano Si half cell with CMC-Na and PAA binders

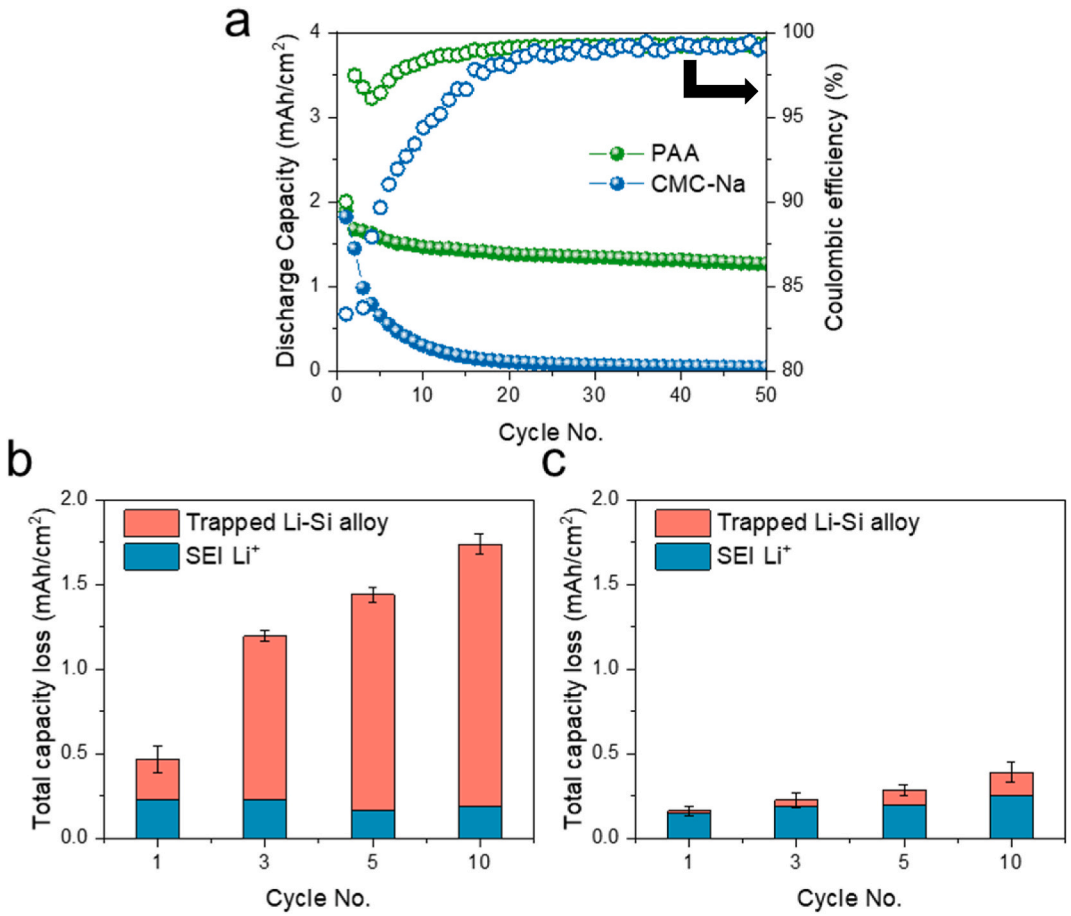

Fig. 3. (a) Cycle performance of CMC-Na and PAA half cells: Trapped Li–Si alloy and SEI Li^+ from TGC results for total capacity loss from different cycles of (b) CMC-Na and (c) PAA half-cell.

after 1 cycle and 5 cycles and the results is summarized in Fig. S3 (c). From the TGC data, it can be seen that for Nano Si with PAA and CMC-Na binders, the trapped Li–Si alloy were 3.08% and 19.05% of the total loss respectively after 1st cycle and 12.74% and 23. 07% of the total loss respectively after 5 cycles. However, in the case of μSi with PAA and CMC-Na binders, the trapped Li–Si alloy were 6.81% and 50.74% of the total loss respectively after 1st cycle and 30.33% and 88.26% of the total loss after 5 cycles (Fig. S3 (d)). The results indicate that trapped Li–Si alloy formation can be further decreased by reducing the particle size of the active material (Si). Many works in the literature have reported that reducing the particle size can increase the density of grain boundaries, improving the Li diffusion kinetics and decreasing the ionic and electronic transport distances [32,33]. This can decrease the trapped Li–Si alloy formation at the particle level which is in agreement with our TGC results.

4.2. SoC effects on Li inventory losses

As previously described, the regions where high volume expansion of μSi occurs should be avoided to limit the amount of trapped Li–Si and SEI formed. This can be achieved by state of charge (SoC) control as the SoC is correlated to the total amount of Li present in the silicon. As SoC control via voltage cutoff is difficult in half cells due to the flat voltage profile of the μSi electrode, full cells with different N/P ratios were assembled to control the SoC. By increasing N/P ratio from 1.5 to 3, the total amount of Li in μSi electrode decrease from 66.67% to 33.33%, as shown in Fig. 4 (a), limits the overall volume expansion of the μSi electrode upon cycling. In this case, both CMC-Na and PAA binders were also used for comparison, and the data are shown in Fig. 4 (b, c). For μSi-CMC-Na//LFP full cells, it can be seen in Fig. 4 (b) that for the N/P ratios 1.5, 2, 2.5, and 3, the ICEs measured were 84.6%, 82.9%, 83.7%, and 81.8%, respectively. As for the cycling performance in Fig. 5 (a), CMC-Na cells using 1.5, 2, 2.5, and 3 as the N/P ratios show the capacity retention 6.9%, 17.2%, 44.8% and 59.7% respectively after 80 cycles and the average CE was 95.6%, 97.3%, 98.8%, 99.1% respectively. However, when the binder was changed to PAA, as shown in Fig. 4 (c), it can be seen that for the N/P ratios: 1.5, 2, 2.5, and 3, the ICE was 84.7%, 82.7%, 81.3%, and 80.9% respectively and from Fig. 5 (b), the capacity retention was 56.9%, 59.7%, 66.6%, 66.6% respectively after 80 cycles and the average CE was 99.2%, 99.3%, 99.4%, 99.4% respectively after 80 cycles. It is worth noting that the average coulombic efficiency still does not reach 99.9% after the improvement, which indicates that other modification methods such as electrolyte or prelithiation need to be further optimized for μSi electrode. All these data sets pointed out that controlling the volume expansion for μSi electrodes is vital toward mitigating trapped Li–Si accumulation in full cells.

TGC tests were further conducted on anodes with different N/P ratios after the 1st and 10th cycles, and the corresponding data are shown in Fig. 5 (c, d). The trapped Li–Si alloy and SEI Li amount here are calculated based on the first charge capacity of the full cell, which is defined as the total Li amount in a full cell with no lithium excess. It shows that SEI was the leading cause of Li inventory loss in full cells at the 1st cycle for CMC-Na and PAA cells that occupied more than 11% of the Li inventory loss, whereas trapped Li–Si amount was negligible (less than 1%). All cells displayed increased Li inventory losses after 10 cycles, with the greatest trapped Li–Si amounts seen in CMC-Na cells, which accounted for more than 23% capacity loss for cell with N/P = 1.5. However, the trapped Li–Si was found to be less than 1.5% when the N/P

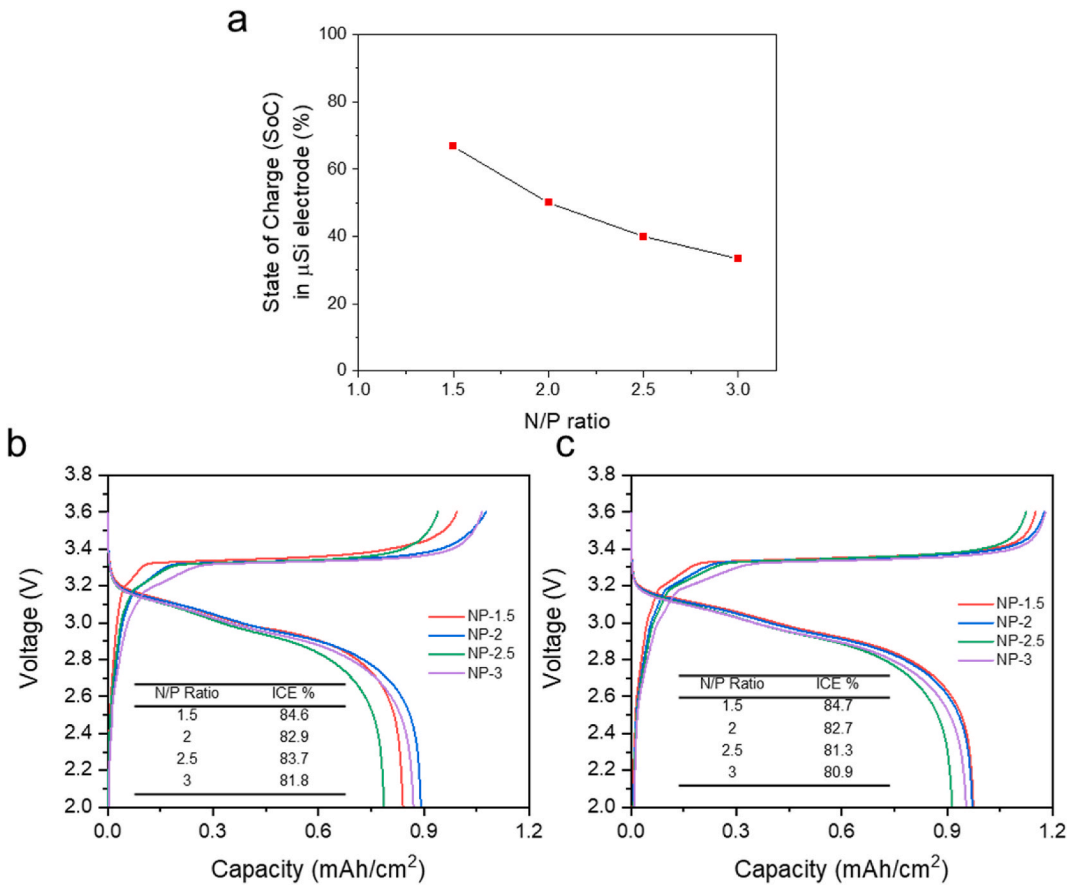

Fig. 4. (a) State of Charge (SoC) v/s N/P ratio plot (b) First Cycle Charge-Discharge profile of μSi-CMC-Na-LFP full cells with various N/P ratios (c) First Cycle Charge-Discharge profile of μSi-PAA-LFP full cells with various N/P ratios.

ratio was increased to 3. Meanwhile, SEI was the primary reason for capacity failure in PAA cells, as trapped Li–Si was significantly lower with less than 3% even for N/P = 1.5. The reduction in trapped Li–Si when N/P ratio was increased from 1.5 to 3 for CMC-Na binder was due to the mild volume expansion-contraction in the μSi anode caused by reduction in State of Charge (SoC) from 66.67% to 33.33%. This was analogous to the lithiation capacity control study in μSi-CMC-Na half cells discussed previously (Fig. 2c). The surface SEM image of μSi anodes for N/P = 1.5 and 3 with CMC-Na binder after 20 cycles (Fig. S6: (a-d)) reveals that cracks are observed on μSi-CMC-Na anode from N/P = 1.5 full cell and cracks are absent on μSi-CMC-Na anode from N/P = 3 full cell. The results further confirms that severe volume expansion-contraction damages the μSi-CMC-Na anode from N/P = 1.5 full cell, potentially leading to electrical isolation and increased trapped Li–Si alloy. Based on these TGC results, the PAA binder can reduce generation and accumulation of trapped Li–Si compared to CMC-Na.

To further investigate the large disparities between CMC-Na and PAA, a 180° peel-off test was performed to compare their binding strengths respectively. The schematic of the test is shown in Fig. S7 (a). The load-displacement plot is shown in Fig. S7 (b). It can be observed that the average load experienced by the PAA electrode was 2.89 N for a displacement range of 50 mm. In contrast, the average load experienced by the CMC-Na electrode was only 0.68 N. Moreover, very little electrode material was peeled off from the copper current collector in the case of the PAA electrode, as shown in Fig. S7 (c), compared to the CMC-Na electrode, even with a higher average load of 2.89 N. From the test results, it can be inferred that the PAA electrode has higher adhesion strength than the CMC-Na electrode. Thus, the PAA binder binds the active material and conducting agent with current collector more effectively than the CMC-Na binder, resulting in less trapped Li–Si.

This study quantitatively analyzed the effect of the state of charge (SoC) control and type of binder on reducing the Li inventory losses in μSi anodes. It showed that trapped Li–Si was the primary cause for Li inventory loss, a result of electronic isolation of active materials during severe volume change in the electrode. This trapped Li–Si accumulation can be mitigated when PAA binder is used instead of CMC-Na. Additionally, state of charge (SoC) control was shown to improve capacity loss by avoiding regions of large volume expansion experienced in the electrode. In the full cell, this was achieved by controlling the N/P ratio. While this quantification study shines light on the root causes of capacity fade with respect to trapped Li–Si or SEI formation, and how it can be mitigated with robust binders and SoC control, full cells with no lithium excess still show significant capacity fade especially over 100 cell cycles. To enable μSi electrodes in practical LIBs, alternative strategies must still be developed to reduce or completely eliminate these effects over extended cell cycling.

5. Conclusions

In conclusion, Trapped Li–Si and SEI were quantified in μSi anode using the Titration Gas Chromatography (TGC) in both half-cell and full cell systems. It was found that SEI formation occurs at the onset of lithiation (until 0.15 V), only after which does the formation of Li–Si alloy occur. Non-linear volume expansion of the μSi anode was observed using both SEM imaging as well as the TGC method, which leads to an increase in rate of SEI formation at regions of high-volume expansion. The quantification results for μSi anode half-cells and full cells showed that trapped Li–Si is the primary reason for the capacity fade, and that it can be mitigated if PAA binder is used instead of CMC-Na. By tuning N/P ratios in full cells, SoC control can be achieved to reduce Li inventory

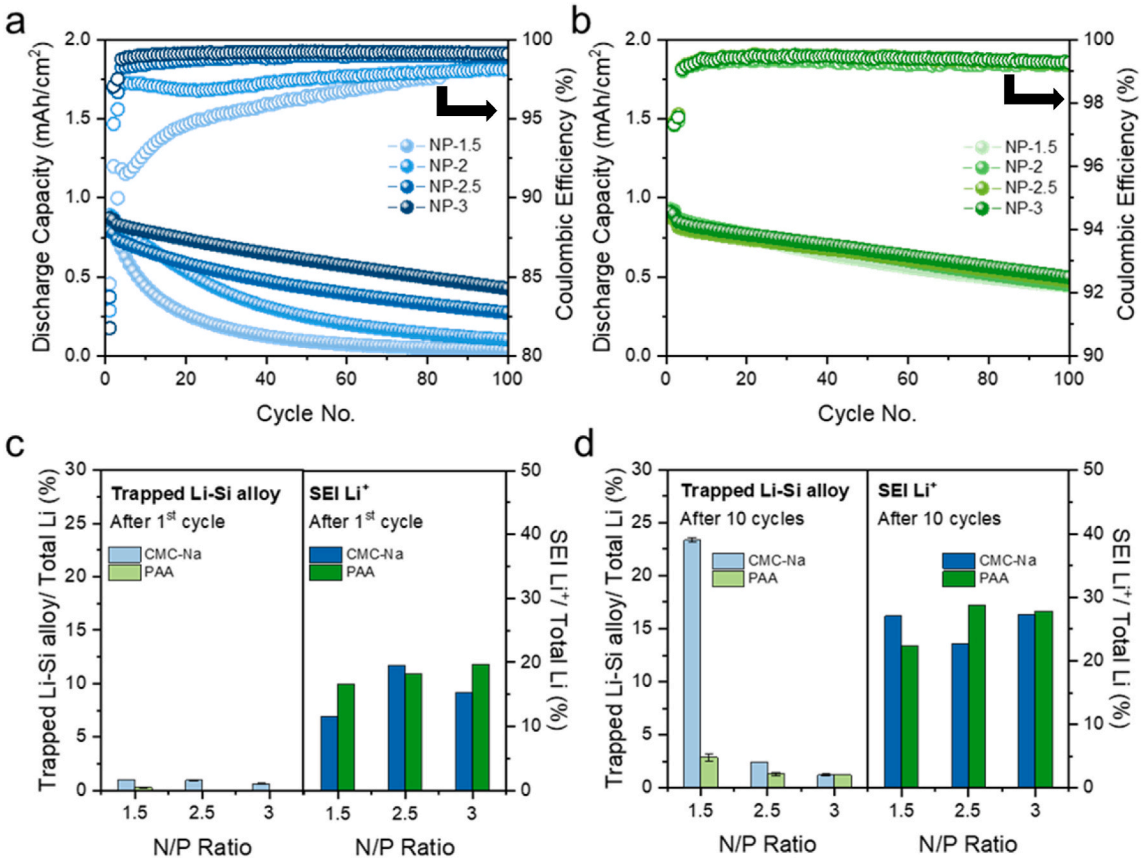

Fig. 5. (a) Cycle performance of μSi- CMC-Na-LFP full-cell with various N/P ratios (b) Cycle performance of μSi-PAA-LFP full-cell with various N/P ratios (c) TGC Data for Lithium inventory loss of full cell after 1st cycle for various N/P ratios (d) TGC Data for Lithium inventory loss of full cell after 10 cycles for various N/P ratios.

losses. A significant decrease in trapped Li–Si over extended cycling was observed when the N/P ratio increased from 1.5 to 3 in the case of full cells with CMC-Na binder. The results in this work demonstrates the capability of the TGC quantification tool to analyze Li inventory losses in μSi anodes, and serves as validation for TGC method applications in other alloy-based anode systems.

CRediT authorship contribution statement

Bhagath Sreenarayanan: Data curation, Investigation, Writing – original draft. **Darren H.S. Tan:** Writing – review & editing. **Shuang Bai:** Writing – review & editing. **Weikang Li:** Investigation, Formal analysis, Writing – review & editing. **Wurigumula Bao:** Conceptualization, Methodology, Investigation, Writing – review & editing. **Ying Shirley Meng:** Conceptualization, Supervision, Writing – review & editing.

Declaration of competing interest

The authors declare that they have no known competing financial interests or personal relationships that could have appeared to influence the work reported in this paper.

Acknowledgements

The authors gratefully acknowledge funding supported by the Ford University Research Program. The SEM was performed at the San Diego Nanotechnology Infrastructure (SDNI) of UCSD, a member of the National Nanotechnology Coordinated Infrastructure supported by the National Science Foundation (Grant ECCS-1542148). Electrochemical testing was performed on a battery test station donated by NeWare.

Appendix A. Supplementary data

Supplementary data to this article can be found online at https://doi.org/10.1016/j.jpowsour.2022.231327.

References

[1] H. Shobukawa, J. Shin, J. Alvarado, C.S. Rustomji, Y.S. Meng, Electrochemical reaction and surface chemistry for performance enhancement of a Si composite anode using a bis(fluorosulfonyl)imide-based ionic liquid, J. Mater. Chem. 4 (2016).
[2] M. Ashuri, Q. He, L.L. Shaw, Silicon as a potential anode material for Li-ion batteries: where size, geometry and structure matter, Nanoscale 8 (2016).
[3] X. Zuo, J. Zhu, P. Müller-Buschbaum, Y.-J. Cheng, Silicon based lithium-ion battery anodes: a chronicle perspective review, Nano Energy 31 (2017).
[4] J.W. Choi, D. Aurbach, Promise and reality of post-lithium-ion batteries with high energy densities, Nat. Rev. Mater. 1 (2016).
[5] M.T. McDowell, et al., Studying the kinetics of crystalline silicon nanoparticle lithiation with in situ transmission electron microscopy, Adv. Mater. 24 (2012).
[6] Z. Ma, et al., Critical silicon-anode size for averting lithiation-induced mechanical failure of lithium-ion batteries, RSC Adv. 3 (2013).
[7] M.T. McDowell, S.W. Lee, W.D. Nix, Y. Cui, Understanding the lithiation of silicon and other alloying anodes for lithium-ion batteries, Adv. Mater. 25 (2013), 25th Anniversary Article.
[8] M.-S. Wang, W.-L. Song, L.-Z. Fan, Three-Dimensional interconnected network of graphene-wrapped silicon/carbon nanofiber hybrids for binder-free anodes in lithium-ion batteries, Chemelectrochem 2 (2015).
[9] M. Raić, et al., Nanostructured silicon as potential anode material for Li-ion batteries, Molecules 25 (2020).
[10] Y. Oumellal, et al., The failure mechanism of nano-sized Si-based negative electrodes for lithium ion batteries, J. Mater. Chem. 21 (2011).
[11] J. Lu, T. Wu, K. Amine, State-of-the-art characterization techniques for advanced lithium-ion batteries, Nat. Energy 2 (2017).
[12] J. Gonzalez, et al., Three dimensional studies of particle failure in silicon based composite electrodes for lithium ion batteries, J. Power Sources 269 (2014).

[13] C. Stetson, et al., Three-dimensional electronic resistivity mapping of solid electrolyte interphase on Si anode materials, Nano Energy 55 (2019).
[14] J. Nanda, et al., Unraveling the nanoscale heterogeneity of solid electrolyte interphase using tip-enhanced Raman spectroscopy, Joule 3 (2019).
[15] G.M. Veith, et al., Determination of the solid electrolyte interphase structure grown on a silicon electrode using a fluoroethylene carbonate additive, Sci. Rep. 7 (2017).
[16] K. Feng, et al., Silicon-based anodes for lithium-ion batteries: from fundamentals to practical applications, Small 14 (2018).
[17] Z. Favors, et al., Towards scalable binderless electrodes: carbon coated silicon nanofiber paper via Mg reduction of electrospun SiO2 nanofibers, Sci. Rep. 5 (2015).
[18] Y. Son, et al., Quantification of pseudocapacitive contribution in nanocage-shaped silicon–carbon composite anode, Adv. Energy Mater. 9 (2019).
[19] B. Jiang, et al., Dual core–shell structured Si@SiO $_x$ @C nanocomposite synthesized via a one-step pyrolysis method as a highly stable Anode material for lithium-ion batteries, ACS Appl. Mater. Interfaces 8 (2016).
[20] Y. Li, et al., Growth of conformal graphene cages on micrometre-sized silicon particles as stable battery anodes, Nat. Energy 1 (2016).
[21] R. Jung, et al., Consumption of fluoroethylene carbonate (FEC) on Si-C composite electrodes for Li-ion batteries, J. Electrochem. Soc. 163 (2016).
[22] K. Schroder, et al., The effect of fluoroethylene carbonate as an additive on the solid electrolyte interphase on silicon lithium-ion electrodes, Chem. Mater. 27 (2015).
[23] M. Nie, et al., Effect of vinylene carbonate and fluoroethylene carbonate on SEI formation on graphitic anodes in Li-ion batteries, J. Electrochem. Soc. 162 (2015).
[24] G.-B. Han, M.-H. Ryou, K.Y. Cho, Y.M. Lee, J.-K. Park, Effect of succinic anhydride as an electrolyte additive on electrochemical characteristics of silicon thin-film electrode, J. Power Sources 195 (2010).
[25] F. Aupperle, et al., The role of electrolyte additives on the interfacial chemistry and thermal reactivity of Si-Anode-Based Li-ion battery, ACS Appl. Energy Mater. 2 (2019).
[26] I. Kovalenko, et al., A major constituent of Brown algae for use in high-capacity Li-ion batteries, Science 334 (2011).
[27] B. Koo, et al., A highly cross-linked polymeric binder for high-performance silicon negative electrodes in lithium ion batteries, Angew. Chem. Int. Ed. 51 (2012).
[28] T. Kwon, et al., Systematic molecular-level design of binders incorporating Meldrum's acid for silicon anodes in lithium rechargeable batteries, Adv. Mater. 26 (2014).
[29] M. Wu, et al., Toward an ideal polymer binder design for high-capacity battery anodes, J. Am. Chem. Soc. 135 (2013).
[30] W. Bao, et al., Quantifying lithium loss in amorphous silicon thin-film anodes via titration-gas chromatography, Cell Rep. Phys. Sci. 2 (2021).
[31] E. Radvanyi, E. de Vito, W. Porcher, S. Jouanneau Si Larbi, An XPS/AES comparative study of the surface behaviour of nano-silicon anodes for Li-ion batteries, J. Anal. At. Spectrom. 29 (2014) 1120–1131.
[32] X. Zhao, V.-P. Lehto, Challenges and prospects of nanosized silicon anodes in lithium-ion batteries, Nanotechnology 32 (2021), 042002.
[33] W.-R. Liu, et al., Effect of electrode structure on performance of Si anode in Li-ion batteries: Si particle size and conductive additive, J. Power Sources 140 (2005) 139–144.